# Extreme material parameters accessible by active acoustic metamaterials with Willis coupling

Steven R. Craig, Bohan Wang, Xiaoshi Su, et al.

Citation: The Journal of the Acoustical Society of America **151**, 1722 (2022); doi: 10.1121/10.0009771
View online: https://doi.org/10.1121/10.0009771
View Table of Contents: https://asa.scitation.org/toc/jas/151/3
Published by the Acoustical Society of America

---

---

JASA ARTICLE

# Extreme material parameters accessible by active acoustic metamaterials with Willis coupling

Steven R. Craig,[1] Bohan Wang,[1] Xiaoshi Su,[2] Debasish Banerjee,[2,a)] Phoebe J. Welch,[1] Mighten C. Yip,[1] Yuhang Hu,[1,b)] and Chengzhi Shi[1,b),c)]

[1]*George W. Woodruff School of Mechanical Engineering, Georgia Institute of Technology, Atlanta, Georgia 30332, USA*

[2]*Toyota Research Institute of North America, 1555 Woodridge Avenue, Ann Arbor, Michigan 48105, USA*

**ABSTRACT:**
Active acoustic metamaterials incorporate electric circuit elements that input energy into an otherwise passive medium to aptly modulate the effective material properties. Here, we propose an active acoustic metamaterial with Willis coupling to drastically extend the tunability of the effective density and bulk modulus with the accessible parameter range enlarged by at least two orders of magnitude compared to that of a non-Willis metamaterial. Traditional active metamaterial designs are based on local resonances without considering the Willis coupling that limit their accessible effective material parameter range. Our design adopts a unit cell structure with two sensor-transducer pairs coupling the acoustic response on both sides of the metamaterial by detecting incident waves and driving active signals asymmetrically superimposed onto the passive response of the material. The Willis coupling results from feedback control circuits with unequal gains. These asymmetric feedback control circuits use Willis coupling to expand the accessible range of the effective density and bulk modulus of the metamaterial. The extreme effective material parameters realizable by the metamaterials will remarkably broaden their applications in biomedical imaging, noise control, and transformation acoustics-based cloaking.
https://doi.org/10.1121/10.0009771

(Received 27 September 2021; revised 18 February 2022; accepted 21 February 2022; published online 16 March 2022)

[Editor: Badreddine Assouar] Pages: 1722–1729

## I. INTRODUCTION

Acoustic metamaterial research aims to develop artificial materials with effective material properties that go beyond what is found in nature to enable superior control over sound wave propagation for applications in biomedical imaging (Fenster *et al.*, 2001; Bushberg and Boone, 2011; Hynynen *et al.*, 1996; Tanter and Fink, 2014; Wang *et al.*, 2016; Errico *et al.*, 2015), noise control (Ma *et al.*, 2014; Li and Assouar, 2016; Mei *et al.*, 2012; Yang *et al.*, 2017), and cloaking technologies (Chen and Chan, 2010; Craster and Guenneau, 2012; Li and Pendry, 2008; Popa *et al.*, 2011; Zheng *et al.*, 2014; Dubois *et al.*, 2017). Although passive metamaterials have adequately demonstrated these unique features, their undesired lossy behavior, narrow bandwidth, and lack of tunability limits their effectiveness for practical applications (Cummer *et al.*, 2016). Active metamaterials compensate for these disadvantages by modulating the additional energy inputs with electrical circuits (Fleury *et al.*, 2015; Zhu *et al.*, 2014). These circuits are highly tunable and can be adjusted in real time because of the swift processing speeds in electrical circuits comparing with the acoustic frequencies, allowing the development of active metasurfaces for reconfigurable focusing and beam steering (Popa *et al.*, 2015). This tunability of active metamaterials was used to modulate the effective density through simple alterations of their active circuitry (Akl and Baz, 2012). Elastic metamaterials with active piezoelectric elements enable the control of different wave characteristics without changing material or structural parameters for transformation-based cloaking (Ning *et al.*, 2020a), elastic black holes (Ning *et al.*, 2020b), and topological immunity on elastic surfaces (Li *et al.*, 2020). Additionally, active metamaterials can achieve negative effective material parameters by actively manipulating the monopole and dipole resonant responses of the unit cells (Popa *et al.*, 2013; Cho *et al.*, 2020).

While existing active metamaterials overcome many disadvantages of their passive counterparts, they were all based on the local resonance of their unit cells that limit the available effective parameter range, making them unsuitable for applications that require extreme effective densities and/or bulk moduli such as transformation acoustics-based cloaking (Popa *et al.*, 2011; Zheng *et al.*, 2014; Dubois *et al.*, 2017), wave steering with extreme angles (Torrent, 2018), and ultrathin sound isolators (Popa *et al.*, 2018). In this study, we propose an active metamaterial with strong Willis coupling to dramatically broaden the accessible range of the effective density and bulk modulus by at least two orders of magnitude compared to that of a non-Willis active metamaterial with a symmetric control circuit. Willis coupling, analogous to bianisotropy in electromagnetics, is a

---

[a)] ORCID: 0000-0003-2402-2944.

[b)] Also at: Parker H. Petit Institute for Bioengineering and Bioscience, Georgia Institute of Technology, Atlanta, GA 30332, USA.

[c)] Electronic mail: chengzhi.shi@me.gatech.edu, ORCID: 0000-0003-0799-213X.

cross coupling of the pressure and local particle velocity fields that couples the monopolar and dipolar responses of metamaterial unit cells (Willis, 1997; Milton and Willis, 2007; Willis, 1981; Willis, 2011; Sieck *et al.*, 2017). These coupled responses result in asymmetric wave propagation to realize ultrathin nonreciprocal sound isolators, abnormal acoustic metagratings with high efficiency, and decorated membranes with large Willis coupling (Zhai *et al.*, 2019; Craig *et al.*, 2019; Chiang *et al.*, 2020; Lau *et al.*, 2019). Additionally, passive acoustic scatterers with maximum Willis coupling overcome inherent efficiency limitations of conventional metasurfaces for arbitrary wavefront manipulation (Quan *et al.*, 2018). Besides fluid media that only support longitudinal waves, Willis coupling metamaterials were used to achieve asymmetric shear wave and asymmetric longitudinal wave propagation in elastic media (Chen *et al.*, 2020). PT-symmetric acoustics is an alternative method that enables asymmetric wave scattering by pairing materials with acoustic gain and loss properties (Liu *et al.*, 2020; Zhu *et al.*, 2014; Schindler *et al.*, 2011). Active Willis coupled metamaterials are also used to study virtualized unit cells for non-reciprocal, non-Hermitian, and topological systems (Cho *et al.*, 2020; Cho *et al.*, 2021; Wen *et al.*, 2021). It is worth noting that asymmetric wave propagation is not the focus of this work. In general, Willis coupling is qualitatively understood as two different types of coupling mechanisms (Sieck *et al.*, 2017). The first, known as even coupling, is present when the geometric center and center of mass are offset, such that any resultant motion from an external force is a combination of the monopolar and dipolar responses (Sieck *et al.*, 2017). The even coupling purely depends on the local properties of the metamaterial and has no reliance on the incident wave. The second, known as odd coupling, exhibits non-local effects due to its dependence on the incident wavevector (Sieck *et al.*, 2017). It is difficult to distinguish the local or non-local behavior in Willis metamaterials, but the presence of Willis coupling extends the range of effective density and bulk modulus (Merkel *et al.*, 2018; Groby *et al.*, 2021).

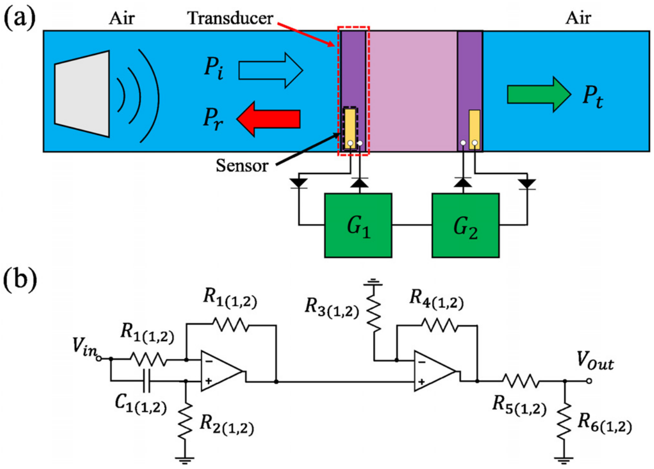

FIG. 1. (Color online) Designed unit cell with active feedback control with Willis coupling when $G_1 \neq G_2$. (a) One-dimensional representation of the metamaterial confined in a waveguide with the active sensor-transducer pairs connected to the feedback control circuits. (b) Active circuitry comprising each gain function for independent control of the phase and amplitude of $G_1$ and $G_2$. (1,2) in the subscripts of the circuit components denote the resistance or capacitance values for $G_1$ and $G_2$, respectively.

## II. MODELING

We model the wave scattering of an active acoustic metamaterial with Willis coupling by decomposing the total acoustic response of the unit cell into its passive and active components as

$$R_{tot} = R_{pass} + R_{act}, \tag{1a}$$

$$T_{tot} = T_{pass} + T_{act}, \tag{1b}$$

where $R_{tot}$ and $T_{tot}$, $R_{pass}$ and $T_{pass}$, and $R_{act}$ and $T_{act}$ are the total, passive, and active acoustic reflection and transmission coefficients, respectively. In this work, we implement a similar passive structure consisting of an air layer [light purple part in Fig. 1(a) represented by the large rectangle between the two thinner rectangles] sandwiched by two piezoelectric transducers [dark purple parts in Fig. 1(a) represented by the thin rectangles on both sides of the larger rectangle] and acoustic sensors [gold parts in Fig. 1(a) represented by the small rectangles contained within the thin rectangles] used in Popa *et al.* (2013). The passive reflection and transmission coefficients were measured in Popa *et al.* (2013) using a 1D waveguide with rectangular cross section when the active circuit components were off. We can control the total acoustic response of the metamaterial by modulating the active response. Our design introduces active control with two sensor-transducer pairs on both sides of the proposed unit cell to detect incident waves and superimpose an active acoustic signal through asymmetric feedback control circuits on the passive acoustic response of the structure [Fig. 1(a)]. Note that the 1D waveguide has hard-wall boundary conditions on the boundaries in parallel to the wave propagation that serve as perfectly reflecting/mirror boundaries and span the single unit cell effectively into a 2D array. Given this setup, the active acoustic outputs are (Popa *et al.*, 2013)

$$R_{L_{act}} = \frac{h_i h_{ro} G_1}{1 - h_{io} G_1}, \tag{2a}$$

$$R_{R_{act}} = \frac{h_i h_{ro} G_2}{1 - h_{io} G_2}, \tag{2b}$$

$$T_{act} = \frac{h_i h_{ro} G_1}{1 - h_{io} G_1} \cdot \frac{h_i h_{to} G_2}{1 - h_{io} G_2}, \tag{2c}$$

where $G_1$ and $G_2$ are the gain functions of the feedback circuit, $R_{R_{act}}$ and $R_{L_{act}}$ are the active acoustic reflection coefficients when an incident wave propagates from the right and left, respectively, $h_i$ is the efficiency that converts a measured input pressure to an input voltage by the sensors, $h_{io}$ is the ratio between the voltage sent out from the driving transducer and the detected voltage received by the sensor, $h_{ro}$ is the efficiency that converts an output voltage to output active reflected pressure, and $h_{to}$ is the efficiency that converts an output voltage to output active transmitted pressure. Since the sensor-transducer pairs are identical, the efficiency terms satisfy the condition $h_{ro} = h_{to}$. These efficiency terms fully characterize the coupling between the mechanical and electrical components in the metamaterial as they quantify the voltage to pressure and voltage to voltage conversions that occur in the active feedback loops. The efficiency terms can be measured following the procedure in Popa *et al.* (2013). For our numerical models, we use the experimentally determined passive material parameters and efficiency terms obtained in Popa *et al.* (2013). Based on Eqs. (2a)–(2c), the active transmission and reflection of the metamaterial can be directly controlled by the gain functions $G_1$ and $G_2$. These gain functions can be realized by the active circuits shown in Fig. 1(b). The resistance and capacitance values of the active circuitry that are required to achieve the desired $G_1$ and $G_2$ are calculated in the supplemental material.[1]

Independent control of the gain functions $G_1$ and $G_2$ allows for the realization of unit cells with or without Willis coupling. In acoustics, Willis coupling is the cross coupling of the pressure and local particle velocity fields, which appears in the constitutive relations as (Sieck *et al.*, 2017; Muhlestein *et al.*, 2017)

$$\mu = \rho v + \tilde{\psi}\frac{\partial \varepsilon}{\partial t}, \tag{3}$$

$$-p = \kappa \varepsilon + \psi \frac{\partial v}{\partial t}, \tag{4}$$

where $\mu$ is the momentum density, $\rho$ is the mass density, $v$ is the particle velocity, $\varepsilon$ is the volume strain, $p$ is the acoustic pressure, $\kappa$ is the bulk modulus, and $\tilde{\psi}$ and $\psi$ are the Willis coupling coefficients. The Willis coupling coefficients are proportional to an asymmetry coefficient $W = \psi\omega/Z$, where $Z$ is the characteristic impedance (Muhlestein *et al.*, 2017). This asymmetry coefficient modifies the specific acoustic impedances $Z_{sp}^{\pm} = Z(1 \pm iW)$, where the positive/negative sign indicates the wave propagation in the forward/backward direction. $W$ can be calculated by the asymmetric acoustic reflection coefficients from the left $R_L$ and from the right $R_R$ and the transmission coefficient $T$ as

$$W = \pm \frac{R_L - R_R}{i\sqrt{\left(1 - R_L R_R + T^2\right)^2 - 4T^2}}, \tag{5}$$

where $R_L$, $R_R$, and $T$ are calculated by substituting Eq. (2) into Eq. (1). This equation indicates that Willis coupling is present with asymmetric acoustic reflection (Muhlestein *et al.*, 2017). Equations (2a) and (2b) illustrate that the introduction of unequal gain functions $G_1$ and $G_2$ result in asymmetric acoustic reflections and, by extension, Willis coupling. Alternatively, this implies that non-Willis media require the gain functions to satisfy $G_1 = G_2$. This non-Willis gain function condition ensures symmetric feedback control circuits and equal reflection coefficients for an acoustic signal incident on either side of the metamaterial.

To determine the effective properties of the active unit cell with Willis coupling for the calculation of accessible material parameter range, we use a generalized parameter retrieval method based on the reflection coefficients $R_L$ and $R_R$, the transmission coefficient $T$, and the passive length of the unit cell derived in Muhlestein *et al.* (2017).

## III. RESULTS

We retrieve the effective density and bulk modulus of a unit cell with and without Willis coupling for $G_1 = 2e^{i(0.87)}$ to investigate the effect of Willis coupling on the effective density and bulk modulus from 2.00 to 3.00 kHz. As previously mentioned, our model uses the efficiency terms and passive material parameters from Popa *et al.* (2013) with $\rho_{pass} = (15 - 4i)\rho_{air}$ and $\kappa_{pass} = (1.15 - 0.3i)\kappa_{air}$, as well as a material thickness $d = 5$ mm and air as the background medium ($\rho_{air} = 1.225\,\mathrm{kg/m^3}$ and $\kappa_{air} = 1.41 \times 10^5$ Pa). Figure 2(a) shows the arithmetic mean of the imaginary part of the asymmetry coefficient, $W$, as a function of the amplitude and phase of $G_2$ near 2.50 kHz calculated from Eqs. (1), (2), and (5). The arithmetic mean is given by the average value of $\mathrm{Im}(W)$ over 2.45 to 2.55 kHz. The non-Willis case occurs when $G_1 = G_2 = 2e^{i(0.87)}$, and is achieved with the active circuitry in Fig. 1(b). The complex effective density and bulk modulus normalized to air of the non-Willis case exhibit frequency bands of negative effective density from 2.85 to 3.00 kHz and negative effective bulk modulus from 2.92 to 3.00 kHz [Fig. 2(b)]. A Willis coupling case is achieved when $G_1 \neq G_2$, where we set $G_1 = 2e^{i(0.87)}$ and $G_2 = 0.6e^{i(2.79)}$. The selection of the amplitude and phase of $G_2$ for the Willis coupled metamaterial is based on the magnitude of the imaginary part of the asymmetry coefficient [Fig. 2(a)] that indicates a large change in the specific acoustic impedance. The complex effective density and bulk modulus normalized to air for this Willis coupling case exhibit a frequency band with negative effective density from 2.33 to 2.63 kHz and negative effective bulk modulus from 2.34 to 2.68 kHz [Fig. 2(c)]. The effective density and bulk modulus achieve a larger magnitude when the imaginary part of the asymmetry coefficient is non-zero [Fig. 2(c)] comparing with the non-Willis coupling case. A second Willis coupling case sets $G_1 = 2e^{i(0.87)}$ and $G_2 = 0.15e^{i(4.10)}$. In this case, the selection of the amplitude and phase of $G_2$ for the Willis coupled metamaterial is based on the magnitude of the imaginary part of the asymmetry coefficient [Fig. 2(a)]. The complex effective density and bulk modulus normalized to air for this Willis coupling case exhibit a frequency band with negative effective bulk modulus from 2.68 to 2.91 kHz [Fig. 2(d)]. The magnitudes of the effective density and bulk modulus increase to even higher values when the imaginary part of the asymmetry coefficient increases its magnitude [Fig. 2(d)]. These two Willis coupling cases suggest an expansion of the range of realizable effective material parameter magnitudes as compared to the non-Willis counterpart.

To determine the accessible parameter range of our active metamaterial with and without Willis coupling, we

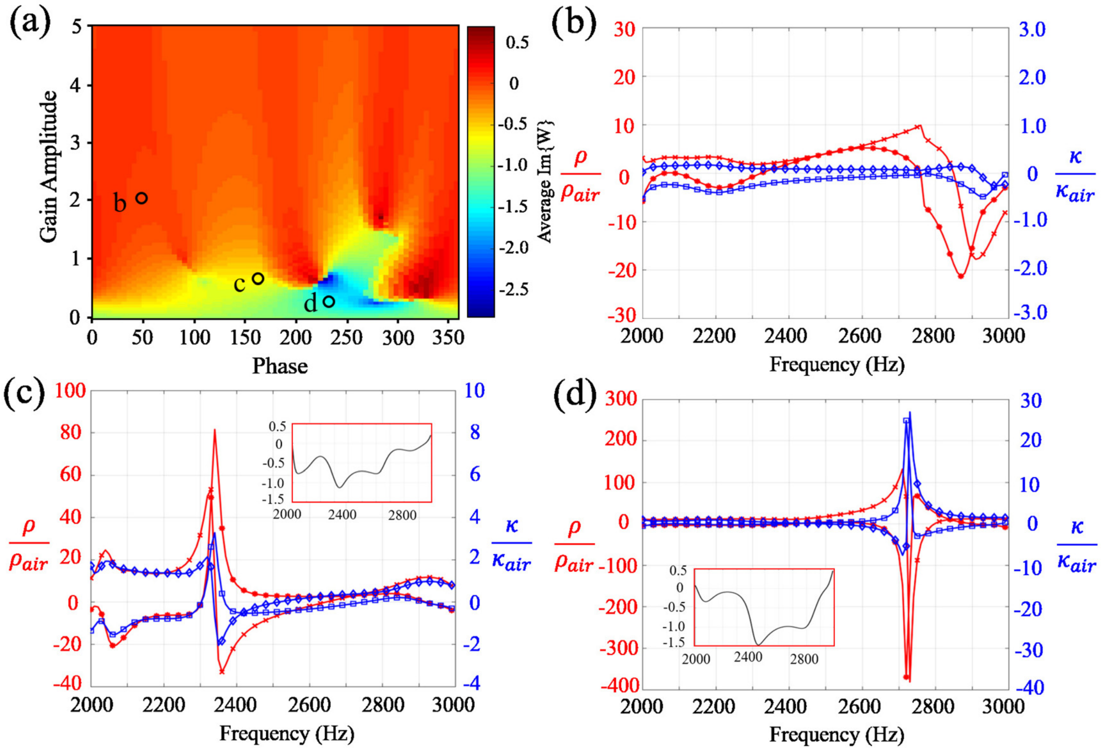

FIG. 2. (Color online) Effects of Willis coupling on effective material parameters. (a) The arithmetic mean of the imaginary part of the asymmetry coefficient as a function of the amplitude and phase of $G_2$ near 2.50 kHz. The three marked points correspond to (b), (c), and (d), respectively. The highest value of the arithmetic mean is shown by the color map in red while the lowest value of the arithmetic mean is shown by the color map in blue. (b) The complex effective density and bulk modulus normalized to air without Willis coupling when $G_1 = G_2 = 2e^{i(0.87)}$. (c) The complex effective density and bulk modulus normalized to air with Willis coupling when $G_1 = 2e^{i(0.87)}$ and $G_2 = 0.6e^{i(2.79)}$. (d) The complex effective density and bulk modulus normalized to air with Willis coupling when $G_1 = 2e^{i(0.87)}$ and $G_2 = 0.15e^{i(4.10)}$. In (b) and (c), the blue diamond and blue square lines plot the real and imaginary bulk modulus, respectively and the red x and red star lines plot the real and imaginary density, respectively. The subplots in (c) and (d) display the corresponding asymmetry coefficient of the Willis coupled metamaterial from 2.00 to 3.00 kHz.

independently vary the phase of the gain functions $G_1$ and $G_2$ from $[0, 2\pi]$ and the amplitude of the gain functions $G_1$ and $G_2$ from [0, 5] and retrieve the effective density and bulk modulus at 2.97 kHz. This frequency corresponds to the monopolar resonance of the non-Willis case when $G_1 = G_2 = 1$. This monopolar resonance will occur at other frequencies when the complex gain functions vary for the non-Willis case. Thus, the selection of frequency is not critical to our results. The active metamaterial without Willis coupling maintains a symmetric feedback circuit with $G_1 = G_2$, while the active metamaterial with Willis coupling has an asymmetric feedback circuit with $G_1 \neq G_2$. We discretize our parameter sweep of the two gain functions with step sizes of 0.005 and 10° for the amplitude and phase changes over the proposed range. The full range of the real-valued effective material parameters are plotted in Fig. 3(a) with the effective density on the horizontal axis and effective bulk modulus on the vertical axis; the black and colored dots correspond to the retrieved material perimeters for the non-Willis and Willis coupling cases, respectively. In the most extreme cases, the available range of the real part of the effective density and bulk modulus with the active Willis coupled metamaterial spans three orders of magnitude beyond the effective parameter range of the non-Willis metamaterial, while the majority of densely clustered points surpass the non-Willis effective range by two orders of magnitude. The outermost points shown in Fig. 3(a) are due to the satisfaction of a resonance condition where the imaginary part of the asymmetry coefficient reaches a local maximum and the real part reaches a local minimum.

The effective density and bulk modulus of these outermost points are very sensitive to any circuit parameter variations. An extreme point in the fourth quadrant of Fig. 3(a) is achieved when $G_1 = 3.025e^{i(4.36)}$ and $G_2 = 2.12e^{i(2.18)}$ resulting in a normalized effective density and bulk modulus $Re(\rho) = 5.39 \times 10^5$ and $Re(\kappa) = -1.81 \times 10^4$. An extreme point in the third quadrant of Fig. 3(c) with the largest magnitude of the negative imaginary part of the effective density is achieved when $G_1 = 4.20e^{i(3.67)}$ and $G_2 = 2.095e^{i(3.84)}$ resulting in a normalized effective density and bulk modulus $Im(\rho) = -1.24 \times 10^5$ and $Im(\kappa) = -1.18 \times 10^3$. While these extreme density and bulk modulus values are three orders higher than the non-Willis case, small variations in the resistance and capacitance values of the active circuits caused by typical manufacturing error results in significant drop (less than an order) to these extreme effective material parameter values (see supplementary material[1]).

For close inspection of the region of densely clustered points, we zoom in on the plot in Fig. 3(a) with the vertical and horizontal axes displaying a normalized density range

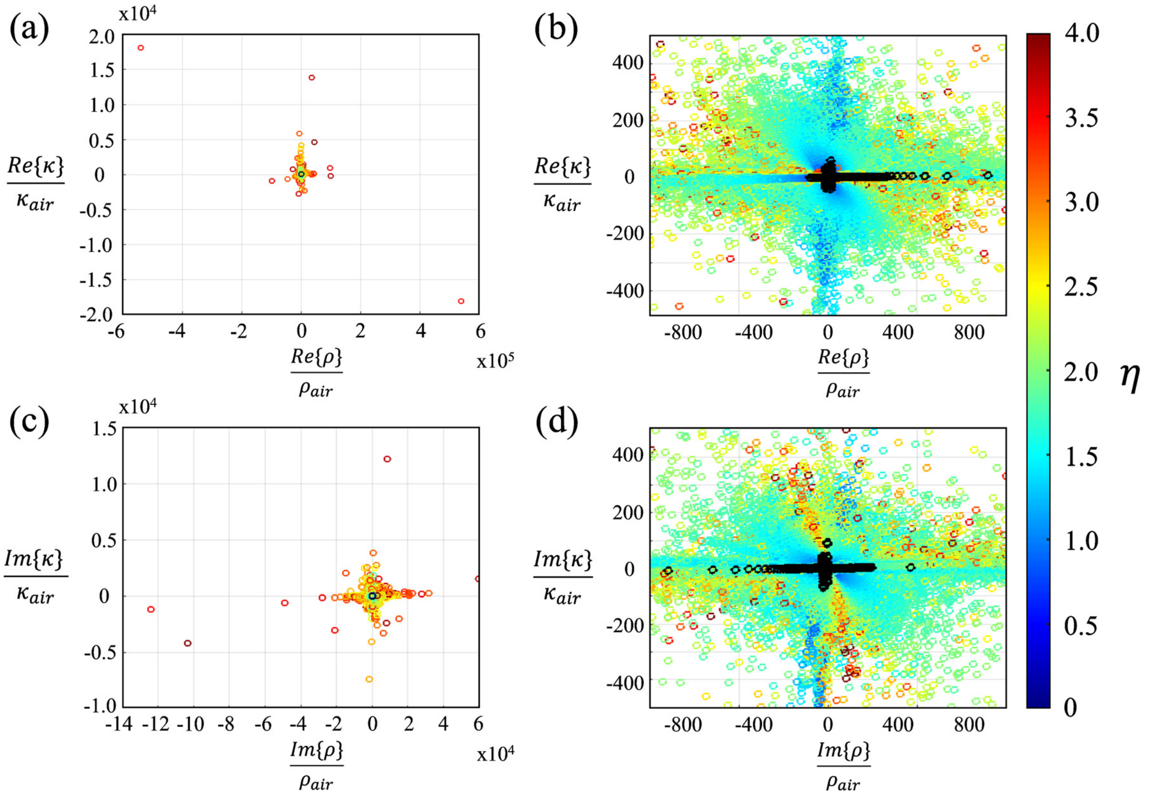

FIG. 3. (Color online) Full effective parameter map of the complex density and bulk modulus for the active Willis coupled and non-Willis metamaterials. (a) Parameter map of the real part of the effective density and bulk modulus for the active metamaterial with and without Willis coupling. The real part of the effective density and bulk modulus are plotted on the horizontal and vertical axes, respectively. Additionally, the colored points and black points represent effective material parameters for Willis and non-Willis metamaterials, respectively. The color map quantifies the logarithm of the ratio of the imaginary part to the real part of the asymmetry coefficient, $\eta = \log_{10}(Abs(Im\{W\}/Re\{W\}))$. The highest value of ($\eta$) is illustrated by the color map as red while the lowest value of ($\eta$) is illustrated by the color map as blue. (b) Magnified window of (a) displaying a normalized density range of [–1000, 1000] and a normalized bulk modulus range of [–500, 500]. (c) Parameter map of the imaginary part of the effective density and bulk modulus for the active metamaterial with and without Willis coupling. The imaginary part of the effective density and bulk modulus are plotted on the horizontal and vertical axes, respectively. This subfigure has the same color scheme as (a). (d) Magnified window of (c) displaying a normalized density range of [–1000, 1000] and a normalized bulk modulus range of [–500, 500].

of [–1000, 1000] and a normalized bulk modulus range of [–500, 500] [Fig. 3(b)]. In this magnified window, all of the resultant parameter values from every possible non-Willis configuration are present. The full parameter range of the non-Willis configurations is completely covered by the Willis coupling cases' point density, indicating that the achievable effective density and bulk modulus of the non-Willis case is fully accessible by the active Willis coupled metamaterial. The real-valued effective density and bulk modulus range resulted from every active Willis coupled metamaterial drastically exceeds the non-Willis metamaterial parameter range by at least two orders of magnitude, both in the positive and negative directions. Similarly, we plot the full range and a magnified window of the imaginary part of the effective material parameters in Figs. 3(c) and 3(d) with the effective density on the horizontal axis and the effective bulk modulus on the vertical axis and the colored and black dots corresponding to the active metamaterial with and without Willis coupling, respectively. The available range of the imaginary parts of the effective density for the active metamaterial with Willis coupling spans about three orders of magnitude beyond the non-Willis metamaterial in the most extreme points, while the majority of points in Fig. 3(c) span two orders of magnitude beyond the non-Willis metamaterial. The imaginary part of the bulk modulus for the active metamaterial with Willis coupling spans one order of magnitude beyond the non-Willis metamaterial. Figure 3(d) zooms in on the plot of Fig. 3(c) to the same parameter range as Fig. 3(b), where all of the resultant parameter values from every non-Willis configuration are present. Similarly, the imaginary part of the non-Willis parameters is fully accessible by the active Willis coupled metamaterial with a broader range and higher resolution. Thus, the accessible range of the imaginary part of the effective density and bulk modulus is much larger and denser with the active Willis coupled metamaterial as compared to the non-Willis metamaterial.

Each point in the Willis case with effective density and bulk modulus values that exceed the effective parameter range of the non-Willis case has a large imaginary part and a small real part of the asymmetry coefficient. Because of the asymmetric active components used in the metamaterial, the extreme effective material parameters result from the presence of Willis coupling. This dramatic effective parameter expansion is illustrated by the color map in Fig. 3, which shows the logarithm of the ratio of the imaginary part of the asymmetry coefficient to the real part of the asymmetry coefficient, $\eta$. The points with extreme effective parameter values have a much larger $\eta$ than those within the vicinity of the non-Willis case (Fig. 3). This result indicates that the cause of the significant parameter range expansion is dominated by the imaginary part of the asymmetry coefficient.

To investigate the effect of the expanded accessible effective density and bulk modulus range on the wave propagation through the active metamaterial, we also calculate the effective refractive index and acoustic impedance normalized to air for our active metamaterial with and without Willis coupling at 2.97 kHz. The full range of the real parts of the effective refractive index and acoustic impedance are shown in Fig. 4(a) with the effective refractive index on the horizontal axis and effective acoustic impedance on the vertical axis. The black and colored dots correspond to the retrieved material parameters for the non-Willis and Willis coupling cases, respectively. While the available range of the real effective impedance ratio with Willis coupling spans three orders of magnitude more than the non-Willis cases in the most extreme points, the majority of densely clustered points span two orders of magnitude beyond the non-Willis case. The available range of the real part of the effective refractive index in both Willis and non-Willis cases are the same. The real part of the refractive index limits are identical due to the branch section of the arccosine function in the parameter retrieval method based on the deep subwavelength passive thickness of the metamaterial. A magnified window with the vertical axis displaying a normalized impedance of [–100, 100] [Fig. 4(b)] confirms that the range of the impedance of the active Willis coupled metamaterial dramatically exceeds the accessibility of the non-Willis cases. This three-order expansion of the acoustic impedance range (two orders for the denser points) aligns with the range expansion of the effective density and bulk modulus, because $Z = \sqrt{\rho\kappa}$. The larger range of the acoustic impedance can result in stronger impedance mismatch between the Willis coupled metamaterial and the background medium to form an ultrathin acoustic barrier with perfect sound isolation (Zhai *et al.*, 2019). The lack of values in the double negative quadrant in Figs. 4(a) and 4(b) stems from the simultaneous negativity of the effective density, bulk modulus, and the resultant negative phase velocity $c$. By defining a characteristic impedance $Z = \rho c$ a negative density and phase velocity result in a positive acoustic impedance.

We show the full range and a magnified window of the imaginary part of the effective refractive index and acoustic impedance in Figs. 4(c) and 4(d) with the effective refractive index on the horizontal axis and the effective acoustic

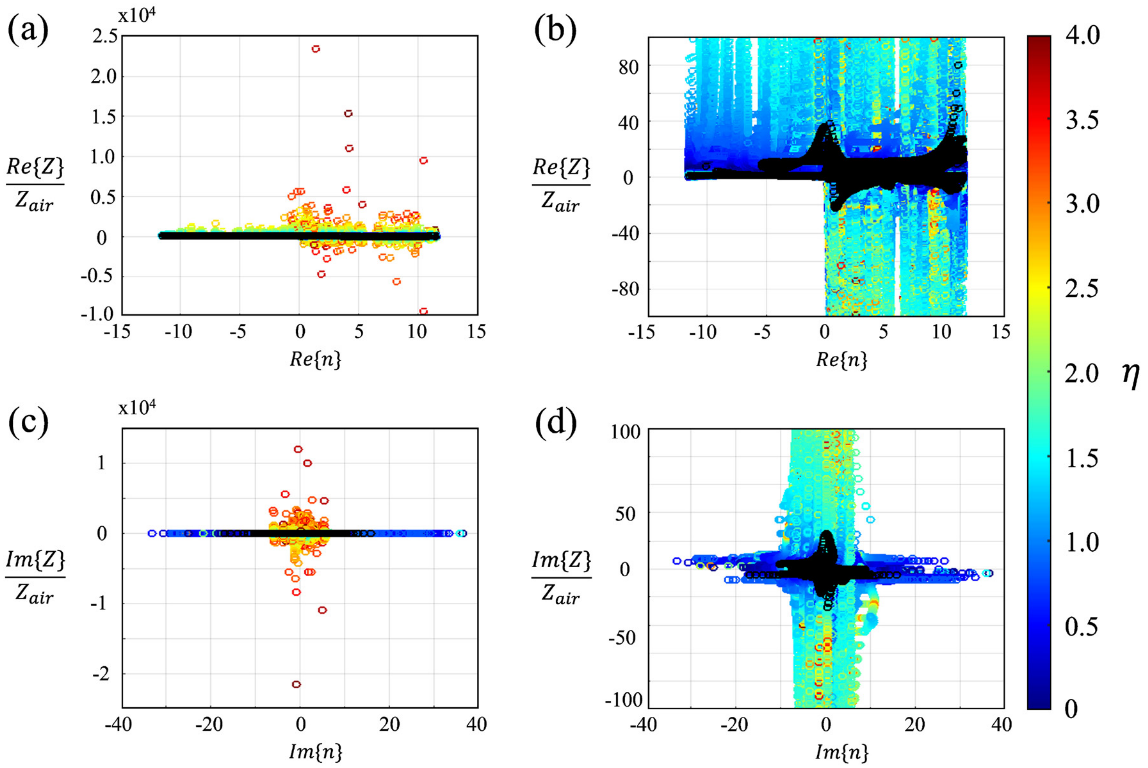

FIG. 4. (Color online) Full parameter map of the complex effective refractive index and acoustic impedance normalized to air for the active Willis coupled and non-Willis metamaterials. (a) The real part of the effective refractive index and acoustic impedance for the active metamaterial with and without Willis coupling. The real part of the effective refractive index and acoustic impedance are plotted on the horizontal and vertical axes, respectively. Additionally, the colored points and black points represent effective material parameters for Willis and non-Willis metamaterials, respectively. The color map quantifies the logarithm of the ratio of the imaginary part to the real part of the asymmetry coefficient, $\eta = \log_{10}(Abs(Im\{W\}/Re\{W\}))$. The highest value of ($\eta$) is illustrated by the color map as red while the lowest value of ($\eta$) is illustrated by the color map as blue. (b) Magnified window of (a) displaying an acoustic impedance range of [–100, 100]. (c) The imaginary part of the effective refractive index and acoustic impedance for the active metamaterial with and without Willis coupling. The imaginary part of the effective refractive index and acoustic impedance are plotted on the horizontal and vertical axes, respectively. This subfigure has the same color scheme as (a). (d) Magnified window of (c) displaying an acoustic impedance range of [–100, 100].

impedance on the vertical axis; the colored and black dots correspond to the active metamaterial with and without Willis coupling, respectively. The available range of the imaginary part of the effective acoustic impedance for the active metamaterial with Willis coupling spans about four orders of magnitude beyond its non-Willis counterpart in the most extreme cases. The majority of points in Fig. 4(c) that correspond to the Willis coupled metamaterial span two orders of magnitude beyond the points that correspond to the non-Willis case. The imaginary part of the refractive index for the Willis cases expands the range of the non-Willis cases by a factor of 2. This broadened range of accessible points in the imaginary part of the refractive index implies an enhanced control of the acoustic loss and gain properties of the metamaterial. Figure 4(d) zooms in on the plot of Fig. 4(c) with the vertical axis displaying a normalized impedance of [–100, 100] to confirm that the range of the impedance for the active metamaterial with Willis coupling achieves high accessibility, dramatically extending beyond the range of the non-Willis metamaterial. Similar to the expanded range of the complex effective density and bulk modulus, the expanded range of the complex acoustic impedance also results from the prevalence of the imaginary part of the asymmetry coefficient, as shown in the color map of $\eta$ in Fig. 4. The expanded ranges of the complex refractive index and acoustic impedance offer superior control of acoustic wave propagation through the active Willis coupled metamaterial.

## IV. CONCLUSION

In conclusion, active metamaterials with Willis coupling dramatically increase the accessible range of the effective density and bulk modulus by at least two orders of magnitude as compared to the accessibility of their non-Willis counterpart. In the most extreme cases, the complex effective density and bulk modulus for active metamaterials with Willis coupling extend the parameter range beyond the non-Willis case by three orders of magnitude. Similar range expansion is observed in the complex acoustic impedance. The parameter range expansion is dominated by the imaginary part of the asymmetry coefficient of the Willis coupling. The development of active metamaterials with extreme material parameters via Willis coupling will enable improved control over acoustic propagation and will yield valuable advancements in biomedical imaging, noise control, and invisibility cloaking technology.

## ACKNOWLEDGMENT

We thank the NSF for the support of this work under Grant No. CMMI-2037565.

[1] See supplementary material at https://www.scitation.org/doi/suppl/10.1121/10.0009771 for discussions on the circuit design, circuit error, and quality factor.

Akl, W., and Baz, A. (**2012**). "Experimental characterization of active acoustic metamaterial cell with controllable dynamic density," J. Appl. Phys. **112**, 084912.

Bushberg, J. T., and Boone, J. M. (**2011**). *The Essential Physics of Medical Imaging* (Lippincott Williams & Wilkins, Philadelphia, PA).

Chen, H., and Chan, C. T. (**2010**). "Acoustic cloaking and transformation acoustics," J. Phys. D: Appl. Phys. **43**, 113001.

Chen, Y., Li, X., Hu, G., Haberman, M. R., and Huang, G. (**2020**). "An active mechanical Willis meta-layer with asymmetric polarizabilities," Nat. Commun. **11**, 1–8.

Chiang, Y. K., Oberst, S., Melnikov, A., Quan, L., Marburg, S., Alù, A., and Powell, D. A. (**2020**). "Reconfigurable acoustic metagrating for high-efficiency anomalous reflection," Phys. Rev. Appl. **13**, 064067.

Cho, C., Wen, X., Park, N., and Li, J. (**2020**). "Digitally virtualized atoms for acoustic metamaterials," Nat. Commun. **11**, 1–8.

Cho, C., Wen, X., Park, N., and Li, J. (**2021**). "Acoustic Willis meta-atom beyond the bounds of passivity and reciprocity," Commun. Phys. **4**, 1–8.

Craig, S. R., Su, X., Norris, A., and Shi, C. (**2019**). "Experimental realization of acoustic bianisotropic gratings," Phys. Rev. Appl. **11**, 061002.

Craster, R. V., and Guenneau, S. (**2012**). *Acoustic Metamaterials: Negative Refraction, Imaging, Lensing and Cloaking* (Springer Science & Business Media, New York).

Cummer, S. A., Christensen, J., and Alù, A. (**2016**). "Controlling sound with acoustic metamaterials," Nat. Rev. Mater. **1**, 1–13.

Dubois, M., Shi, C., Wang, Y., and Zhang, X. (**2017**). "A thin and conformal metasurface for illusion acoustics of rapidly changing profiles," Appl. Phys. Lett. **110**, 151902.

Errico, C., Pierre, J., Pezet, S., Desailly, Y., Lenkei, Z., Couture, O., and Tanter, M. (**2015**). "Ultrafast ultrasound localization microscopy for deep super-resolution vascular imaging," Nature **527**, 499–502.

Fenster, A., Downey, D. B., and Cardinal, H. N. (**2001**). "Three-dimensional ultrasound imaging," Phys. Med. Biol. **46**, R67–99.

Fleury, R., Sounas, D., and Alu, A. (**2015**). "An invisible acoustic sensor based on parity-time symmetry," Nat. Commun. **6**, 1–7.

Groby, J. P., Malléjac, M., Merkel, A., Romero-García, V., Tournat, V., Torrent, D., and Li, J. (**2021**). "Analytical modeling of one-dimensional resonant asymmetric and reciprocal acoustic structures as Willis materials," New J. Phys. **23**, 053020.

Hynynen, K., Freund, W. R., Cline, H. E., Chung, A. H., Watkins, R. D., Vetro, J. P., and Jolesz, F. A. (**1996**). "A clinical, noninvasive, MR imaging-monitored ultrasound surgery method," Radiographics **16**, 185–195.

Lau, J., Tang, S. T., Yang, M., and Yang, Z. (**2019**). "Coupled decorated membrane resonators with large Willis coupling," Phys. Rev. Appl. **12**, 014032.

Li, G. H., Ma, T. X., Wang, Y. Z., and Wang, Y. S. (**2020**). "Active control on topological immunity of elastic wave metamaterials," Sci. Rep. **10**, 9376.

Li, J., and Pendry, J. B. (**2008**). "Hiding under the carpet: A new strategy for cloaking," Phys. Rev. Lett. **101**, 203901.

Li, Y., and Assouar, B. M. (**2016**). "Acoustic metasurface-based perfect absorber with deep subwavelength thickness," Appl. Phys. Lett. **108**, 063502.

Liu, T., Ma, G., Liang, S., Gao, H., Gu, Z., An, S., and Zhu, J. (**2020**). "Single-sided acoustic beam splitting based on parity-time symmetry," Phys. Rev. B **102**, 014306.

Ma, G., Yang, M., Xiao, S., Yang, Z., and Sheng, P. (**2014**). "Acoustic metasurface with hybrid resonances," Nat. Mater. **13**, 873–878.

Mei, J., Ma, G., Yang, M., Yang, Z., Wen, W., and Sheng, P. (**2012**). "Dark acoustic metamaterials as super absorbers for low-frequency sound," Nat. Commun. **3**, 1–7.

Merkel, A., Romero-García, V., Groby, J. P., Li, J., and Christensen, J. (**2018**). "Unidirectional zero sonic reflection in passive PT-symmetric Willis media," Phys. Rev. B **98**, 201102.

Milton, G. W., and Willis, J. R. (**2007**). "On modifications of Newton's second law and linear continuum elastodynamics," Proc. R. Soc. A: Math. Phys. **463**, 855–880.

Muhlestein, M. B., Sieck, C. F., Wilson, P. S., and Haberman, M. R. (**2017**). "Experimental evidence of Willis coupling in a one-dimensional effective material element," Nat. Commun. **8**, 1–9.

Ning, L., Wang, Y. Z., and Wang, Y. S. (**2020a**). "Active control cloak of the elastic wave metamaterial," Int. J. Solids Struct. **202**, 126–135.

Ning, L., Wang, Y. Z., and Wang, Y. S. (**2020b**). "Active control of a black hole or concentrator for flexural waves in an elastic metamaterial plate," Mech. Mater. **142**, 103300.

Popa, B.-I., Shinde, D., Konneker, A., and Cummer, S. A. (**2015**). "Active acoustic metamaterials reconfigurable in real time," Phys. Rev. B **91**, 220303.

Popa, B.-I., Zhai, Y., and Kwon, H.-S. (**2018**). "Broadband sound barriers with bianisotropic metasurfaces," Nat. Commun. **9**, 1–7.

Popa, B.-I., Zigoneanu, L., and Cummer, S. A. (**2011**). "Experimental acoustic ground cloak in air," Phys. Rev. Lett. **106**, 253901.

Popa, B.-I., Zigoneanu, L., and Cummer, S. A. (**2013**). "Tunable active acoustic metamaterials," Phys. Rev. B **88**, 024303.

Quan, L., Ra'di, Y., Sounas, D. L., and Alù, A. (**2018**). "Maximum Willis coupling in acoustic scatterers," Phys. Rev. Lett. **120**, 254301.

Schindler, J., Li, A., Zheng, M. C., Ellis, F. M., and Kottos, T. (**2011**). "Experimental study of active LRC circuits with PT symmetries," Phys. Rev. A **84**, 040101.

Sieck, C. F., Alù, A., and Haberman, M. R. (**2017**). "Origins of Willis coupling and acoustic bianisotropy in acoustic metamaterials through source-driven homogenization," Phys. Rev. B **96**, 104303.

Tanter, M., and Fink, M. (**2014**). "Ultrafast imaging in biomedical ultrasound," IEEE. T. Ultrason. Ferroelectr. **61**, 102–119.

Torrent, D. (**2018**). "Acoustic anomalous reflectors based on diffraction grating engineering," Phys. Rev. B **98**, 060101.

Wang, S., Lin, J., Wang, T., Chen, X., and Huang, P. (**2016**). "Recent advances in photoacoustic imaging for deep-tissue biomedical applications," Theranostics **6**, 2394–2413.

Wen, X., Zhu, X., Wu, H. W., and Li, J. (**2021**). "Realizing spatiotemporal effective media for acoustic metamaterials," Phys. Rev. B **104**, L060304.

Willis, J. (**1997**). *Dynamics of Composites*, Vol. 495 of Continuum Micromechanics: CISM Lecture Notes (Springer, Wien), Chap. 1.

Willis, J. R. (**1981**). "Variational principles for dynamic problems for inhomogeneous elastic media," Wave Motion **3**, 1–11.

Willis, J. R. (**2011**). "Effective constitutive relations for waves in composites and metamaterials," Proc. R. Soc. A: Math. Phys. **467**, 1865–1879.

Yang, M., Chen, S., Fu, C., and Sheng, P. (**2017**). "Optimal sound-absorbing structures," Mater. Horiz. **4**, 673–680.

Zhai, Y., Kwon, H.-S., and Popa, B.-I. (**2019**). "Active Willis metamaterials for ultracompact nonreciprocal linear acoustic devices," Phys. Rev. B **99**, 220301.

Zheng, L.-Y., Wu, Y., Ni, X., Chen, Z.-G., Lu, M.-H., and Chen, Y.-F. (**2014**). "Acoustic cloaking by a near-zero-index phononic crystal," Appl. Phys. Lett. **104**, 161904.

Zhu, X., Ramezani, H., Shi, C., Zhu, J., and Zhang, X. (**2014**). "PT-symmetric acoustics," Phys. Rev. X **4**, 031042.